PAPER

Check for updates

Outstanding elastic, electronic, transport and optical properties of a novel layered material C₄F₂: first-principles study

Tuan V. Vu, [iD] [ab] Huynh V. Phuc,[c] Sohail Ahmad,[d] Vo Quang Nha,[e] Chu Van Lanh,[f] D. P. Rai, [iD] [g] A. I. Kartamyshev,[ab] Khang D. Pham,[h] Le Cong Nhan[i] and Nguyen N. Hieu [iD] *[jk]

Motivated by very recent successful experimental transformation of AB-stacking bilayer graphene into fluorinated single-layer diamond (namely fluorinated diamane C_4F_2) [P. V. Bakharev, M. Huang, M. Saxena, S. W. Lee, S. H. Joo, S. O. Park, J. Dong, D. C. Camacho-Mojica, S. Jin, Y. Kwon, M. Biswal, F. Ding, S. K. Kwak, Z. Lee and R. S. Ruoff, Nat. Nanotechnol., 2020, 15, 59–66], we systematically investigate the structural, elastic, electronic, transport, and optical properties of fluorinated diamane C_4F_2 by using density functional theory. Our obtained results demonstrate that at the ground state, the lattice constant of C_4F_2 is 2.56 Å with chemical bonding between the C–C interlayer and intralayer bond lengths of about 1.5 Å which are close to the C–C bonding in the bulk diamond. Based on calculations for the phonon spectrum and ab initio molecular dynamics simulations, the structure of C_4F_2 is confirmed to be dynamically and thermally stable. C_4F_2 exhibits superior mechanical properties with a very high Young's modulus of 493.19 N m^{-1}. Upon fluorination, the formation of C–C bonding between graphene layers has resulted in a comprehensive alteration of electronic properties of C_4F_2. C_4F_2 is a direct semiconductor with a large band gap and phase transitions are found when a biaxial strain or external electric field is applied. Interestingly, C_4F_2 has very high electron mobility, up to 3.03×10^3 cm^2 V^{-1} s^{-1}, much higher than other semiconductor compounds. Our findings not only provide a comprehensive insight into the physical properties of C_4F_2 but also open up its applicability in nanoelectromechanical and optoelectronic devices.

1 Introduction

Graphene, a single layer of atoms forming a two-dimensional (2D) hexagonal lattice,[1] has attracted enormous attention due

[a]Division of Computational Physics, Institute for Computational Science, Ton Duc Thang University, Ho Chi Minh City, Viet Nam. E-mail: vuvantuan@tdtu.edu.vn

[b]Faculty of Electrical & Electronics Engineering, Ton Duc Thang University, Ho Chi Minh City, Viet Nam

[c]Division of Theoretical Physics, Dong Thap University, Cao Lanh 870000, Vietnam

[d]Department of Physics, College of Science, King Khalid University, P.O. Box 9004, Abha, Saudi Arabia. E-mail: sohail@kku.edu.sa

[e]School of Engineering and Technology, Hue University, Hue, Viet Nam

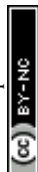[f]Department of Physics, Vinh University, 182 Le Duan, Vinh City, Viet Nam

[g]Physical Sciences Research Center, Department of Physics, Pachhunga University College, Mizoram University, Aizawl 796001, India

[h]Military Institute of Mechanical Engineering, Ha Noi 100000, Viet Nam

[i]Department of Environmental Science, Sai Gon University, Ho Chi Minh City, Viet Nam

[j]Institute of Research and Development, Duy Tan University, Da Nang 550000, Viet Nam

[k]Faculty of Natural Sciences, Duy Tan University, Da Nang 550000, Viet Nam. E-mail: hieunn@duytan.edu.vn

to its exceptional properties, including high mechanical stability,[2,3] extraordinary electronic properties,[4–7] and excellent electrical conductivity.[8–10] However, in the semimetal form with zero band gap, there is some disadvantage for applications of graphene in electronic devices, such as field-effect transistors.[11] Along with finding alternative materials, effective ways to change the electronic structure of graphene have been found, including strain engineering[12] and the formation of graphene-based van der Waals heterostructures.[13–15] Particularly, chemically-induced surface functionalization is found to be one of the most powerful methods to modulate the electron states of graphene.[16,17] The formation of sp³ bonding hybridization due to the chemical functionalization of the surface has given functionalized graphene novel physical properties that are not present in pure graphene (with sp² bonds).[16] One showed that the energy gap of graphene can be turned up to 3.90 eV by hydrogenation of its surface.[18]

Recently, a transformation from bilayer graphene into ultra-thin diamond film (referred to as diamane) by high pressure has been experimentally reported.[19,20] Also, diamane can be experimentally obtained by fully surface-hydrogenation of the AB-stacking bilayer graphene.[21,22] Previously, electron states of

hydrogenated bilayer graphene have been predicted by using density functional theory (DFT).[23] Interestingly, a large band gap is found in the hydrogenated bilayer graphene and its band gap can be controlled by an applied bias voltage between graphene layers.[23] Besides, hydrogenated bilayer graphene C_2H is predicted to have superior mechanical properties with an in-plane stiffness up to 751 N m^{-1}, quite stronger than both graphene and graphane.[24] Diamane based hydrogenated bilayer graphene has also attracted great attention with a series of theoretical studies.[25,26]

A transformation of bilayer graphene into diamane by the high-pressure method may have the problem that after the pressure has been released, diamane can return to the original structure of bilayer graphene. Hence, chemical surface-functionalization is considered the optimal method for multi-layer graphene diamondization. Previous experiment study has been demonstrated that chemical surface functionalization with fluorine atoms is much easier than that with hydrogen atoms due to the difference in electronegativity between fluorine and hydrogen and carbon.[27] Besides, the growth time of graphene in the chemical vapor deposition (CVD) method for the case of functionalization with F is shortened than that with other groups.[28] By using first-principles calculations, Odkhuu *et al.*, demonstrated that fluorination of C atoms at the outer surface can convert AB-stacking (Bernal-type stacking) bilayer graphene into sp^3-bonded diamane with intralayer and inter-layer C–C bond lengths being respectively 1.52 Å and 1.58 Å, which are close to the sp^3 bond length in bulk diamond (1.54 Å).[29] This implies that the C–C bond lengths are similar to that in diamond, suggesting that diamane will possess a large nature band gap and outstanding mechanical properties. *Via* first-principles calculations, Sivek *et al.* demonstrated that chemi-sorption on AB-stacking bilayer graphene is the most energetically favorable and band gap of fluorinated AB-stacking bilayer graphene (4.040 eV) is larger than that of fluorinated monolayer graphene by about 1 eV.[30] Effects of the strain on stability and electronic properties of halogenated diamane have been investigated by the first-principles calculations.[31,32]

Very recently, a transformation of CVD-grown AB-stacking bilayer graphene into a fluorinated single-layer diamond (C_4F_2) has been experimentally reported.[33] Motivated by this successfully experimental synthesis, in this paper, we systematically investigate the structural, elastic, electronic, transport, and optical properties of F-diamane C_4F_2 by using DFT calculations. The structural and mechanical stability of C_4F_2 is carefully investigated. Besides, the influences of strain engineering and electric field on electron states of C_4F_2 are also focused.

2 Computational details

Optimized atomic structures and calculations for electronic characteristics are performed by using the first-principles calculations based on the DFT as implemented in the Quantum Espresso code.[34] The project augmented wave (PAW) method[35] was used to describe the electron–ion core interactions. We used the generalized gradient approximations with exchange–correlation functional of Perdew–Burke–Ernzerhof (PBE).[36] To correct the band structure of investigated systems, the Heyd–Scuseria–Ernzerhof (HSE06) functional[37] was also used. The DFT-D2 method by Grimme[38] was performed to treat the van der Waals interactions in diamane. The plane-wave cut-off energy of 500 eV is used in our calculations. The Brillouin zone is sampled by a (15 × 15 × 1) *k*-mesh. The atomic structures were optimized until the residual forces on atoms were less than 10^{-3} eV Å^{-1}. We set a vertical vacuum space of 20 Å to limit the interlayer interactions. The phonon dispersion relations, which are used to examine the dynamical stability of investigated systems, were calculated using the density functional perturbation theory method[39] *via* the Quantum Espresso package.[34] Besides, the *ab initio* molecular dynamics (AIMD) simulations were performed based on the Nosé thermostat algorithm[40] at room temperature (300 K) for 10 ps with time step of 1 fs to verify the thermal stability of the systems. The canonical ensemble (*NVT*) with fixed particle number, volume and temperature is used in our molecular dynamic simulations. A large supercell of 4 × 4 × 1 which contains 96 atoms (64 C atoms and 32 F atoms) was used for the molecular dynamic simulations to guarantee the convergence and obtain accurate results. The dynamical examinations are begun with the optimized structure of C_4F_2 at 0 K. The mechanical stability of investigated systems was evaluated *via* calculations for the elastic constants and then compared with the Born criteria for mechanical stability.[41]

3 Stability and elastic properties

Single-layer diamond or diamane can be formed from bilayer graphene *via* surface functionalization. Atomic structure of fluorinated diamane C_4F_2 is shown in Fig. 1. The structure of C_4F_2 looks like interlayer bonded bilayer graphene but its interlayer distance is much shorter than that in bilayer graphene. After relaxation, the lattice constant of C_4F_2 is 2.56 Å
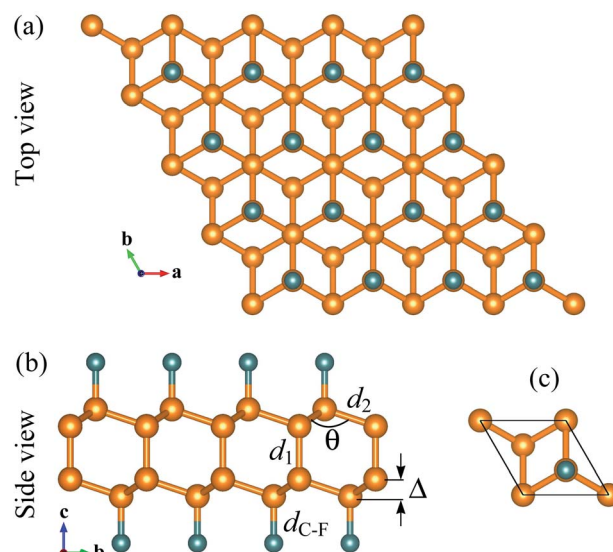

Fig. 1 Different views of optimized atomic structure (a, b) and primitive cell (c) for C_4F_2.

Table 1 Calculated results for lattice parameter a (Å), interlayer C–C bond length d_1 (Å), in-plane C–C bond length d_2 (Å), C–F bond length d_{C-F} (Å), buckling constant Δ (Å), C–C–C bond angle θ (deg.), binding energy E_b (eV), elastic constants C_{ij} (N m^{-1}), Young's modulus Y_{2D} (N m^{-1}), 2D shear modulus G_{2D} (N m^{-1}), and Poisson's ratio ν

	a	d_1	d_2	d_{C-F}	Δ	θ	E_b	C_{11}	C_{12}	Y_{2D}	G_{2D}	ν
C$_4$F$_2$	2.56	1.55	1.56	1.38	0.50	110.17	−44.132	499.46	55.96	493.19	221.75	0.11
	2.56^a	1.55^a	1.56^a	1.38^a	—	110.20^a	—	—	—	—	—	0.10^c
	2.56^b	1.55^b	1.56^a	1.37^b	0.50^b	110.13^b	—	—	—	—	—	—

[a] Ref. 30. [b] Ref. 31. [c] Ref. 32.

which is slightly larger than that of hydrogenated diamane (2.53 Å).[42] The C–C interlayer bond length d_1 and in-plane C–C bond length in C$_4$F$_2$ are found to be 1.55 Å and 1.56 Å, respectively. Our obtained result for the lattice parameters is in good agreement with the previous DFT calculations.[30] Clearly, the C–C interlayer bonding d_1 in C$_4$F$_2$ is much shorter than the interlayer distance in AB-stacking bilayer graphene (about 3.3 Å), implying that the layers in bilayer graphene are held together by the weak van der Waals force rather than by the C–C chemical bond. The calculated structural parameters of fluorinated diamane C$_4$F$_2$ are listed in Table 1.

We next calculate the binding energy to examine the energetic stability. The binding energy E_b of C$_4$F$_2$ can be calculated via expression as:

$$E_b = E_{C_4F_2} - (N_C E_C + N_F E_F), \quad (1)$$

where $E_{C/F}$ is the energy of the single atom C/F, $E_{C_4F_2}$ is the total energy of the C$_4$F$_2$, and $N_{C/F}$ is the number of the C/F atoms in the unitcell. Obtained results demonstrate that the binding energy of C$_4$F$_2$ is $E_b = -44.132$ eV per atom. The negative value of E_b implies that C$_4$F$_2$ is energetically favorable for F to bond with C atoms and one can fabricate C$_4$F$_2$ as free-standing material.

The phonon spectrum of C$_4$F$_2$ is also calculated to test its dynamical stability. The primitive cell of C$_4$F$_2$ contains six atoms. Hence, there are 18 branches in its phonon dispersion relations, including three acoustic branches and 15 optical branches. The calculated phonon spectrum along the Brillouin zone of C$_4$F$_2$ is demonstrated in Fig. 2(a). In the phonon spectrum of C$_4$F$_2$, there is an intersection between acoustic and optical vibrational branches and both acoustic and optical branches coexist in the same phonon frequency. This can lead to strong optical-acoustic scattering and C$_4$F$_2$ may possess low-thermal conductivity as a result of this strong scattering. Also, the highest optical phonon frequency of C$_4$F$_2$ is up to 1300 cm^{-1}, demonstrating that the C–F bonds in C$_4$F$_2$ is strong. Most importantly, there are no soft-modes in the phonon spectrum of the considered system. This implies that C$_4$F$_2$ is dynamically stable. If negative frequencies were present, there would be no restoring forces against the displacement of atoms. Further, the AIMD simulations at room temperature (300 K) within 10 ps with a time step of 1 fs are performed to examine the thermal stability of the considered system. In Fig. 2(b) and (c), we show the calculated results for the fluctuations of total energy and temperature as functions of heating time. As presented in Fig. 2(b) and (c), the total energy of C$_4$F$_2$ is fluctuated very slightly, about 0.5 eV, during the 10 ps of heating at room

temperature. The atomic structure of C$_4$F$_2$ is still robust and there is no structural transition nor bond breaking in the C$_4$F$_2$ structure after being heated for a period of 10 ps as presented in Fig. 2(d). It implies that the thermal stability of C$_4$F$_2$ at room temperature has been verified and it can be used in physical devices.

It is well-known that carbon nanomaterials have outstanding mechanical properties. For insights into the mechanical stability issue, we calculate the elastic properties to examine the mechanical characteristics of C$_4$F$_2$. We use the standard Voigt notation for the elastic constants C_{ij}. For 2D structures, there are four independent elastic constants, including C_{11}, C_{22}, C_{12}, and C_{66}. The elastic constant can be calculated by using DFT calculations. The angular-dependence of the 2D Young's modulus $Y_{2D}(\theta)$ (or in-plane stiffness) and Poisson's ratio $\nu(\theta)$ can be directly derived from the stiffness tensor components C_{ij}[43,44]

$$Y_{2D}(\theta) = \frac{C_{11}C_{22} - C_{12}{}^2}{C_{11}\Delta^4 + C_{22}\Lambda^4 - \Delta^2\Lambda^2\left(2C_{12} - \dfrac{C_{11}C_{22} - C_{12}{}^2}{C_{66}}\right)}, \quad (2)$$

$$\nu(\theta) = \frac{C_{12}(\Delta^4 + \Lambda^4) - \Delta^2\Lambda^2\left(C_{11} + C_{22} - \dfrac{C_{11}C_{22} - C_{12}{}^2}{C_{66}}\right)}{C_{11}\Delta^4 + C_{22}\Lambda^4 - \Delta^2\Lambda^2\left(2C_{12} - \dfrac{C_{11}C_{22} - C_{12}{}^2}{C_{66}}\right)}, \quad (3)$$
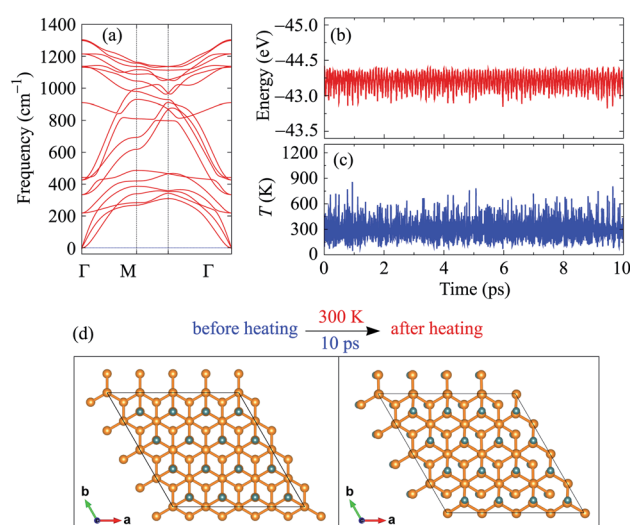

Fig. 2 Stability of C$_4$F$_2$: phonon spectrum (a), AIMD simulations for fluctuations of total energy (b) and temperature (c) as a function time, and snapshots of atomic structure before and after heating at 300 K within 10 ps (d).
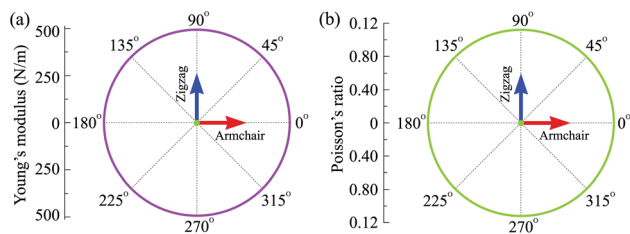
Fig. 3 Polar diagram for the Young's modulus and Poisson's ratio of C_4F_2.

where $\Delta = \sin\theta$ and $\Lambda = \cos\theta$. Here, θ is the angle relative to the armchair direction.

Due to hexagonal structure, in-plane elastic constant $C_{11} = C_{22}$ and we can directly calculate the C_{66} via relationship $C_{66} = (C_{11} - C_{12})/2$. It implies that, for C_4F_2, there are only two nonzero elastic constants to be estimated being C_{11} and C_{12}.

Our calculated results demonstrate that the in-plane elastic constant of C_4F_2 being $C_{11} = 499.46$ N m^{-1} and $C_{12} = 55.96$ N m^{-1}. The obtained values for the elastic constants of C_4F_2, as listed in Table 1, satisfies the Born criteria[41] for mechanical stability with $C_{11} > 0$ and $C_{11}^2 - C_{12}^2 > 0$. Our calculations indicate that the elastic constants of C_4F_2 are greater than most other 2D layered materials, demonstrating the superiority of its mechanical properties. As listed in Table 1, $Y_{2D} = 493.19$ N m^{-1} and $G_{2D} = 221.75$ N m^{-1}, which is comparable to that of graphene (340 N m^{-1} and 144 N m^{-1}, respectively).[45] Also, the Poisson's ratio of C_4F_2 is 0.11 which is close to that of graphene (0.17).[44] Obtained results for elastic constants reflect that C_4F_2 has high in-plane stiffness and strong bonding. The polar diagram for the $Y_{2D}(\theta)$ and $\nu(\theta)$ of C_4F_2 are presented in Fig. 3. We can see that the angle-dependence of $Y_{2D}(\theta)$ and $\nu(\theta)$ of C_4F_2 have perfectly circular shape, reflecting that C_4F_2 has fully isotropic elastic properties.

4 Electronic properties

Graphene and also bilayer graphene are predicted to be semi-metal with a zero band gap.[46] Surface functionalization is an effective way to turn the electronic properties of layered materials. In Fig. 4, we present our calculated results for band

Fig. 4 Band structure and partial density of states (PDOS) of C_4F_2 monolayer.

structure of C_4F_2. Obtained results demonstrated that at the ground state, C_4F_2 is a direct semiconductor with a large energy gap. Both the conduction band minimum (CBM) and valence band maximum (VBM) locate at the Γ point in the first Brillouin zone. The estimated energy gap of C_4F_2 by the PBE functional is 4.13 eV, which is larger than that of both graphane (3.5 eV) and fluorinated graphene (3.1 eV).[47] However, the PBE method is known to be underestimated the energy gap problem of the semiconductor. Hence, to correct the band structure of the investigated system, we also perform the calculations for the band structure of C_4F_2 by using the hybrid functional HSE06. Obtained results indicate that the estimated band structures of C_4F_2 by HSE06 and PBE methods have the same profile. At the HSE06 level, the energy gap of C_4F_2 is up to 5.75 eV as presented in Fig. 4. To explore the contribution of atomic orbital to the band structure formation, we also plot out the partial density of states (PDOS) as shown in Fig. 4. While the CBM of C_4F_2 is mainly contributed by F–s orbitals, the VBM is occupied by the C–p and F–p orbitals. The F–p orbital greatly contributes to the valence band, especially in the region from -3 to -6 eV.

Note that strain engineering is the best way to turn the electronic properties of 2D layered materials. Here, we investigate the dependent-biaxial strain of the electronic properties of C_4F_2. The dependent-biaxial strain is quantitatively investigated via the expression as $\varepsilon_b = (a - a_0)/a_0$. Here, a and a_0 are the lattice constants of the investigated system with and without strain, respectively. In the present study, a large range of biaxial strain from -10 to 10% is applied to the system (minus sign stands for the compressive case). Band structure of C_4F_2 at several values of ε_b is shown in Fig. 5. In the compressive strain case ($\varepsilon_b < 0$) as illustrated in Fig. 5(a), direct semiconductor characteristic of C_4F_2 is preserved, however, its band gap is significantly changed (decreased) when the compressive strain is applied. Interesting takes place in the case of tensile strain ($\varepsilon_b > 0$) where the direct–indirect gap transitions are observed as illustrated in Fig. 5(b). We can reveal that the CBM tends to move from Γ to M point and vice versa when the tensile strain was introduced. Consequently, the indirect–direct gap transitions take place at $\varepsilon_b = +4\%$ and $\varepsilon_b = +10\%$. At $\varepsilon_b = +4\%$, C_4F_2 becomes the indirect semiconducting material with the CBM at the M-point and the indirect semiconductor characteristic of C_4F_2 is prevented in the strain range from +4 to +8% and the indirect–direct energy gap transition occurs again at $\varepsilon_b = +10\%$ the CBM returns to the original point (Γ-point) and the C_4F_2 is the direct semiconductor at $\varepsilon_b = +10\%$.

Along with mechanical strain, the electron states of layered nanomaterials can be modulated by electric gating. In this paper, an electric field E is perpendicularly applied to the surface of investigated material (along c-axes). A plus sign of the electric field E indicates that the $\vec{E}$ direction coincides with the positive direction of the c-axis and vice versa. The band structures of C_4F_2 under the E are shown in Fig. 6. Obtained results reveal that the band structure of C_4F_2 depends greatly on the E. In the presence of the E, there is the redistribution of charge due to the electric field and the polarization of effective charges in the electronic bands will also respond to the external field. Consequently, the electron states of materials can be altered by
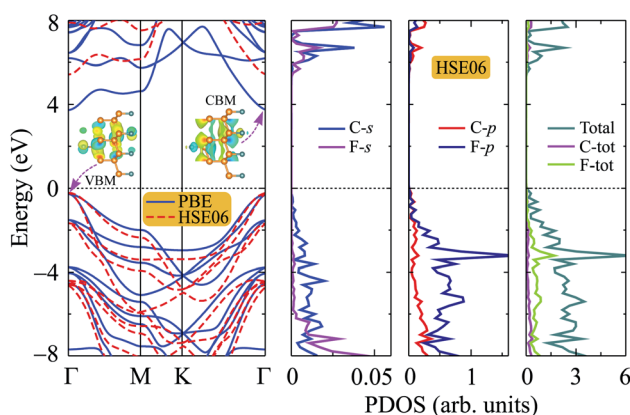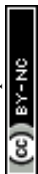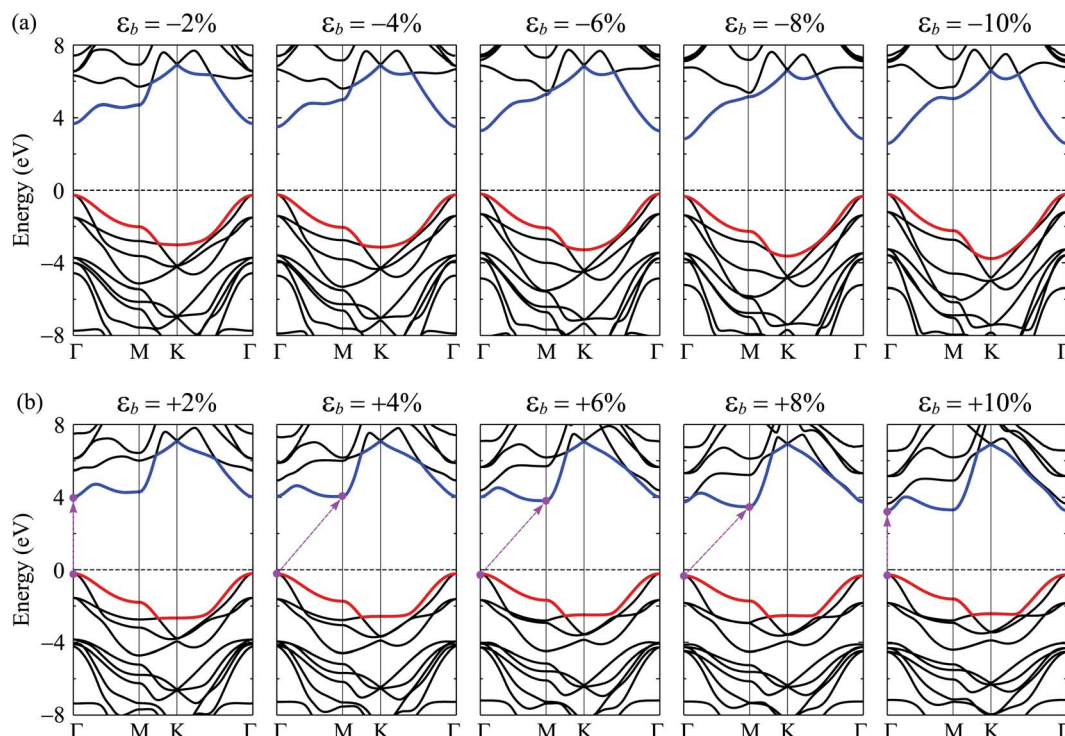
Fig. 5 Band structures of C_4F_2 monolayer under strain: (a) compressive strain $\varepsilon_b < 0$ and (b) tensile strain $\varepsilon_b > 0$.

the external field. Obtained results indicate that the transition from semiconducting to metallic behavior is found in C_4F_2 when the E was introduced. In the presence of the E, the energy gap of C_4F_2 decreases slightly when the E varies from 0 to 2 V nm^{-1}. However, the energy gap reduces quickly with the continued increase in the electric field. Consequently, The semiconductor-to-metal transitions are found at $E = \pm 5$ V nm^{-1}. At $E = \pm 5$ V nm^{-1}, as presented in Fig. 6, the highest
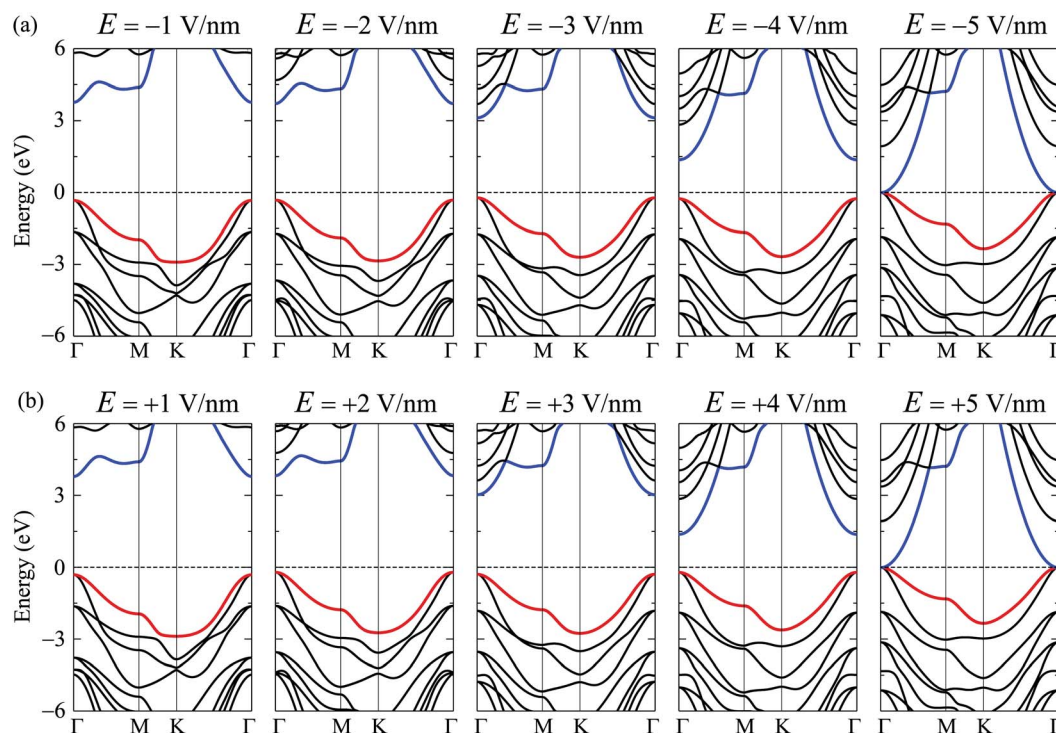

Fig. 6 Band structures of the C_4F_2 in the presence of (a) negative and (b) positive electric fields.
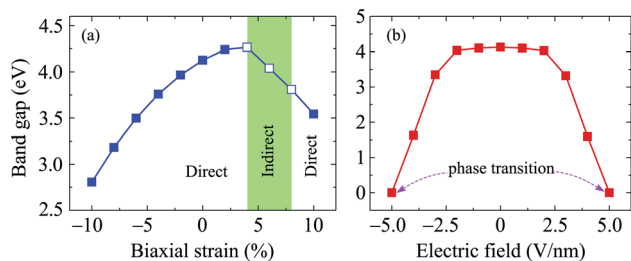
Fig. 7 Band gap of C_4F_2 as a function of a biaxial strain ε_b (a) and an electric field E (b). Filled and empty squares in (a) refer to the direct and indirect gaps, respectively.

subband of the valence band and the lowest subband of the conduction band intersect at the Fermi level (the Fermi level is set at zero) and C_4F_2 becomes a metal. Both the VBM and CBM are always at the Γ-point in the presence of the electric field, implying that C_4F_2 is a direct semiconductor (except the phase transition point at ± 5 V nm^{-1}). The E- and ε_b-dependent band gap of C_4F_2 is depicted in Fig. 7. The energy gap of C_4F_2 decreases quite rapidly (about 32%) in the case of $\varepsilon_b < 0$, from 4.13 eV at equilibrium ($\varepsilon_b = 0$) to 2.81 eV at $\varepsilon_b = -10\%$. For the $\varepsilon_b > 0$ case, the band gap of C_4F_2 slightly increases and then linearly decreases with tensile strain as shown in Fig. 7(a). The electronic properties of 2D nanomaterials are very sensitive to the altering in their structure. When the strain is applied, the bond lengths between atoms in materials are changed, leading to a change in their hopping energy which plays a key role in the modulation of electron states of materials.[48] The semiconductor–metal transition in C_4F_2 due to the external field as shown in Fig. 6 and 7(b) is an important characteristic that makes C_4F_2 promising for applications in nanoelectromechanical devices.

5 Transport properties

The carrier mobility is a key factor determining possibility applicability of materials to electronic devices. The carrier mobility can be studied by using deformation potential approximation.[49] For 2D systems, the carrier mobility μ_{2D} is given by:[50,51]

$$\mu_{2D} = \frac{e\hbar^3 C_{2D}}{k_B T m^* \overline{m} E_d^2}, \quad (4)$$

where e is the electron charge, T is the temperature, C_{2D} and E_d are respectively the elastic modulus and deformation potential constant, m^* and $\overline{m} = \sqrt{m_x^* m_y^*}$ are the carrier effective and average effective masses, respectively.

The effective mass of the carrier is also an important parameter of materials. The carrier effective mass m^* is given by $\frac{1}{m^*} = \frac{1}{\hbar} \frac{\partial^2 E(k)}{\partial k^2}$ with $E(k)$ is the electron energy at a wave vector k at the CBM/VBM. Our obtained results show that, at the CBM, the lateral electron effective masses m_e^* along Γ–K and Γ–M of C_4F_2 are $0.55m_0$ and $0.55m_0$, respectively. Here, m_0 is the free mass of an electron. Meanwhile, at the VBM, the lateral

hole effective masses m_h^* along Γ–K and Γ–M are obtained to be $-1.04m_0$ and $-0.97m_0$, respectively. Consequently, the carrier mobility of C_4F_2 is predicted to be high due to the low carrier effective masses and high elastic modulus C_{11}. At room temperature of 300 K, the electron mobility μ_e of C_4F_2 is found to be 3.03×10^3 cm^2 V^{-1} s^{-1}. Clearly that the electron mobility of our calculated results for the electron mobility of C_4F_2 is comparable with a previous study (2.73×10^3 cm^2 V^{-1} s^{-1}).[52] It is clear that the electron mobility of C_4F_2 is much higher than that of compounds with similar band gap.[53]

6 Optical properties

Besides electronic properties, C_4F_2 possesses interesting optical characteristics that could be useful in performance optical devices. The parameters of optical characteristics can be estimated *via* the dielectric function, which is written as $\varepsilon(\omega) = \varepsilon_1(\omega) + i\varepsilon_2(\omega)$. Here, $\varepsilon_{1/2}(\omega)$ and $\varepsilon_2(\omega)$ is the real/imaginary part of $\varepsilon(\omega)$ at the incident photon frequency ω, respectively. The $\varepsilon_2(\omega)$ is given by[54,55]

$$\varepsilon_2(\omega) = \frac{4\pi^2 e^2}{V m^2 \varpi^2} \sum_{nn'\sigma} \langle kn\sigma | p_i | kn'\sigma \rangle \langle kn'\sigma | p_j | kn\sigma \rangle$$
$$\times f_{kn}(1 - f_{kn'}) \delta(E_{kn'} - E_{kn} - \hbar\omega), \quad (5)$$

where m and e are respectively the mass and charge of an electron, $|knp\rangle$ is the wave-function of the crystal with the momentum operator p, V is the unit-cell volume, and f_{kn} is the Fermi distribution function. We then can obtain $\varepsilon_1(\omega)$ by using the Kramers–Kronig transformation.[56]

The absorption coefficient $A(\omega)$ is given by[57]

$$A(\omega) = \frac{\sqrt{2}\omega}{c} \left[\sqrt{\varepsilon_1(\omega)^2 + \varepsilon_2(\omega)^2} - \varepsilon_1(\omega) \right]^{1/2}. \quad (6)$$

The calculated results for the $\varepsilon(\omega)$ and $A(\omega)$ of C_4F_2 by both PBE and HSE06 approaches are presented in Fig. 8. The static dielectric constant $\varepsilon_1(0)$ of a semiconductor depends strongly on its band gap. This relationship can be described *via* the Penn model.[58] According to the Penn model, the $\varepsilon_1(0)$ is inversely proportional to the direct energy gap of the semiconductor. The $\varepsilon_1(0)$ of C_4F_2 is 1.53 (PBE) and 1.27 (HSE06). As presented in Fig. 8, there is no absorption in the visible light region. This is due to the large band gap of C_4F_2 as above-presented. The
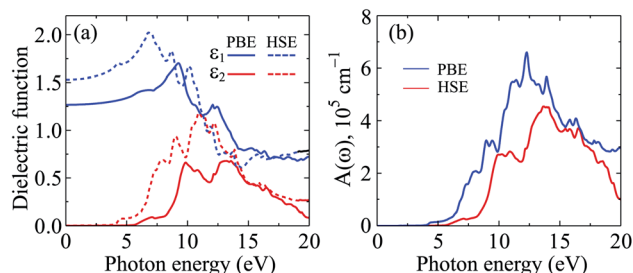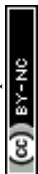

Fig. 8 Calculated dielectric function (a) and absorption coefficient (b) of C_4F_2 by the PBE and HSE06 methods.

optical absorption of C_4F_2 is activated in the ultraviolet region, at 4.13 eV and 5.70 eV respectively by the PBE and HSE06 methods, which is consistent with its direct band gap of C_4F_2 as above-mentioned. After activation, the intensity of the optical absorption of C_4F_2 increases rapidly as presented in Fig. 8(b). C_4F_2 exhibits to have very high absorption intensity in the ultraviolet region. At the PBE level, the maximum absorbance of C_4F_2 is 6.59×10^5 cm^{-1} at the incident photon energy of 12.30 eV. It is noted that the Bethe–Salpeter equation (BSE) on top of the one-shot G_0W_0 calculations (G_0W_0 + BSE method),[47,59,60] which both the electron–electron and electron–hole interactions are taken into account, is considered as the best method to investigate the optical properties of 2D materials. The previous study indicated that the first absorption peak, which is caused by the interband transition, appears at the incident photon energy of 5.47 eV in the absorption spectrum of C_4F_2 by G_0W_0 + BSE method.[31] These results are comparable to our results by the HSE06 calculations.

7 Conclusion

In summary, we have systematically considered the typical properties of fluorinated diamane C_4F_2 by using the DFT calculations. Our findings demonstrated that C_4F_2 is a stable structure with both C–C interlayer and intralayer bond lengths that are similar to C–C bonds in bulk diamond. C_4F_2 exhibits superior mechanical properties with quite high Young's modulus. Also, C_4F_2 has high optical absorbance in the near-ultraviolet light region with a maximum value up to 6.59×10^5 cm^{-1}. Interestingly, C_4F_2 is found to be a semiconductor with a large band gap up to 5.75 eV at the HSE06 level and we can alter its band gap by strain engineering or electric field, especially the semiconductor–metal phase transition is found at $E = \pm 5$ V nm^{-1} which opens up many possibilities for the application of C_4F_2 in electronic devices.

Conflicts of interest

There are no conflicts to declare.

Acknowledgements

References

1 K. S. Novoselov, A. K. Geim, S. V. Morozov, D. Jiang, Y. Zhang, S. V. Dubonos, I. V. Grigorieva and A. A. Firsov, *Science*, 2004, **306**, 666.
2 C. Lee, X. Wei, J. W. Kysar and J. Hone, *Science*, 2008, **321**, 385.
3 B. Hajgató, S. Güryel, Y. Dauphin, J.-M. Blairon, H. E. Miltner, G. Van Lier, F. De Proft and P. Geerlings, *J. Phys. Chem. C*, 2012, **116**, 22608.
4 A. H. Castro Neto, F. Guinea, N. M. R. Peres, K. S. Novoselov and A. K. Geim, *Rev. Mod. Phys.*, 2009, **81**, 109–162.
5 N. A. Poklonski, S. A. Vyrko, A. I. Siahlo, O. N. Poklonskaya, S. V. Ratkevich, N. N. Hieu and A. A. Kocherzhenko, *Mater. Res. Express*, 2019, **6**, 042002.
6 A. I. Siahlo, N. A. Poklonski, A. V. Lebedev, I. V. Lebedeva, A. M. Popov, S. A. Vyrko, A. A. Knizhnik and Y. E. Lozovik, *Phys. Rev. Mater.*, 2018, **2**, 036001.
7 A. D. Phan, N. A. Viet, N. A. Poklonski, L. M. Woods and C. H. Le, *Phys. Rev. B: Condens. Matter Mater. Phys.*, 2012, **86**, 155419.
8 M. Cao, D.-B. Xiong, L. Yang, S. Li, Y. Xie, Q. Guo, Z. Li, H. Adams, J. Gu, T. Fan, X. Zhang and D. Zhang, *Adv. Funct. Mater.*, 2019, **29**, 1806792.
9 A. M. Popov, I. V. Lebedeva, A. A. Knizhnik, Y. E. Lozovik, B. V. Potapkin, N. A. Poklonski, A. I. Siahlo and S. A. Vyrko, *J. Chem. Phys.*, 2013, **139**, 154705.
10 I. V. Lebedeva, A. M. Popov, A. A. Knizhnik, Y. E. Lozovik, N. A. Poklonski, A. I. Siahlo, S. A. Vyrko and S. V. Ratkevich, *Comput. Mater. Sci.*, 2015, **109**, 240.
11 F. Schwierz, *Nat. Nanotechnol.*, 2010, **5**, 487.
12 G. G. Naumis, S. Barraza-Lopez, M. Oliva-Leyva and H. Terrones, *Rep. Prog. Phys.*, 2017, **80**, 096501.
13 K. D. Pham, N. N. Hieu, H. V. Phuc, I. A. Fedorov, C. A. Duque, B. Amin and C. V. Nguyen, *Appl. Phys. Lett.*, 2018, **113**, 171605.
14 C. V. Nguyen, M. Idrees, H. V. Phuc, N. N. Hieu, N. T. T. Binh, B. Amin and T. V. Vu, *Phys. Rev. B*, 2020, **101**, 235419.
15 H. T. T. Nguyen, M. M. Obeid, A. Bafekry, M. Idrees, T. V. Vu, H. V. Phuc, N. N. Hieu, L. T. Hoa, B. Amin and C. V. Nguyen, *Phys. Rev. B*, 2020, **102**, 075414.
16 E. Cadelano, P. L. Palla, S. Giordano and L. Colombo, *Phys. Rev. B: Condens. Matter Mater. Phys.*, 2010, **82**, 235414.
17 A. V. Lebedev, I. V. Lebedeva, A. M. Popov, A. A. Knizhnik, N. A. Poklonski and S. A. Vyrko, *Phys. Rev. B*, 2020, **102**, 045418.
18 J. Son, S. Lee, S. J. Kim, B. C. Park, H.-K. Lee, S. Kim, J. H. Kim, B. H. Hong and J. Hong, *Nat. Commun.*, 2016, **7**, 13261.
19 L. G. P. Martins, M. J. S. Matos, A. R. Paschoal, P. T. C. Freire, N. F. Andrade, A. L. Aguiar, J. Kong, B. R. A. Neves, A. B. de Oliveira, M. S. Mazzoni, A. G. S. Filho and L. G. Cançado, *Nat. Commun.*, 2017, **8**, 96.
20 Y. Gao, T. Cao, F. Cellini, C. Berger, W. A. de Heer, E. Tosatti, E. Riedo and A. Bongiorno, *Nat. Nanotechnol.*, 2018, **13**, 133.
21 F. Piazza, K. Cruz, M. Monthioux, P. Puech and I. Gerber, *Carbon*, 2020, **169**, 129.
22 S. Rajasekaran, F. Abild-Pedersen, H. Ogasawara, A. Nilsson and S. Kaya, *Phys. Rev. Lett.*, 2013, **111**, 085503.
23 D. K. Samarakoon and X.-Q. Wang, *ACS Nano*, 2010, **4**, 4126.
24 L. A. Chernozatonskii, P. B. Sorokin, A. G. Kvashnin and D. G. Kvashnin, *JETP Lett.*, 2009, **90**, 134.
25 O. Leenaerts, B. Partoens and F. M. Peeters, *Phys. Rev. B: Condens. Matter Mater. Phys.*, 2009, **80**, 245422.
26 A. G. Kvashnin, L. A. Chernozatonskii, B. I. Yakobson and P. B. Sorokin, *Nano Lett.*, 2014, **14**, 676.

27 C. Liu, X. Xu, L. Qiu, M. Wu, R. Qiao, L. Wang, J. Wang, J. Niu, J. Liang, X. Zhou, Z. Zhang, M. Peng, P. Gao, W. Wang, X. Bai, D. Ma, Y. Jiang, X. Wu, D. Yu, E. Wang, J. Xiong, F. Ding and K. Liu, *Nat. Chem.*, 2019, **11**, 730.

28 Y. Xie, T. Cheng, C. Liu, K. Chen, Y. Cheng, Z. Chen, L. Qiu, G. Cui, Y. Yu, L. Cui, M. Zhang, J. Zhang, F. Ding, K. Liu and Z. Liu, *ACS Nano*, 2019, **13**, 10272.

29 D. Odkhuu, D. Shin, R. S. Ruoff and N. Park, *Sci. Rep.*, 2013, **3**, 3276.

30 J. Sivek, O. Leenaerts, B. Partoens and F. M. Peeters, *J. Phys. Chem. C*, 2012, **116**, 19240–19245.

31 H. Shu, *J. Mater. Chem. C*, 2021, **9**, 4505–4513.

32 B. Mortazavi, F. Shojaei, B. Javvaji, M. Azizi, H. Zhan, T. Rabczuk and X. Zhuang, *Appl. Surf. Sci.*, 2020, **528**, 147035.

33 P. V. Bakharev, M. Huang, M. Saxena, S. W. Lee, S. H. Joo, S. O. Park, J. Dong, D. C. Camacho-Mojica, S. Jin, Y. Kwon, M. Biswal, F. Ding, S. K. Kwak, Z. Lee and R. S. Ruoff, *Nat. Nanotechnol.*, 2020, **15**, 59–66.

34 P. Giannozzi, S. Baroni, N. Bonini, M. Calandra, R. Car, C. Cavazzoni, D. Ceresoli, G. L. Chiarotti, M. Cococcioni, I. Dabo, A. D. Corso, S. de Gironcoli, S. Fabris, G. Fratesi, R. Gebauer, U. Gerstmann, C. Gougoussis, A. Kokalj, M. Lazzeri, L. Martin-Samos, N. Marzari, F. Mauri, R. Mazzarello, S. Paolini, A. Pasquarello, L. Paulatto, C. Sbraccia, S. Scandolo, G. Sclauzero, A. P. Seitsonen, A. Smogunov, P. Umari and R. M. Wentzcovitch, *J. Phys.: Condens. Matter*, 2009, **21**, 395502.

35 G. Kresse and D. Joubert, *Phys. Rev. B: Condens. Matter Mater. Phys.*, 1999, **59**, 1758.

36 J. P. Perdew, K. Burke and M. Ernzerhof, *Phys. Rev. Lett.*, 1996, **77**, 3865.

37 J. Heyd, G. E. Scuseria and M. Ernzerhof, *J. Chem. Phys.*, 2003, **118**, 8207.

38 S. Grimme, *J. Comput. Chem.*, 2006, **27**, 1787.

39 T. Sohier, M. Calandra and F. Mauri, *Phys. Rev. B*, 2017, **96**, 075448.

40 S. Nosé, *J. Chem. Phys.*, 1984, **81**, 511.

41 F. Mouhat and F.-X. Coudert, *Phys. Rev. B: Condens. Matter Mater. Phys.*, 2014, **90**, 224104.

42 Y. Zhang, C.-H. Hu, Y.-H. Wen, S.-Q. Wu and Z.-Z. Zhu, *New J. Phys.*, 2011, **13**, 063047.

43 N. T. Hung, A. R. T. Nugraha and R. Saito, *J. Phys. D: Appl. Phys.*, 2018, **51**, 075306.

44 P. Xiang, S. Sharma, Z. M. Wang, J. Wu and U. Schwingenschlögl, *ACS Appl. Mater. Interfaces*, 2020, **12**, 30731.

45 T. Cheng, H. Lang, Z. Li, Z. Liu and Z. Liu, *Phys. Chem. Chem. Phys.*, 2017, **19**, 23942.

46 E. McCann and M. Koshino, *Rep. Prog. Phys.*, 2013, **76**, 056503.

47 F. Karlický and M. Otyepka, *J. Chem. Theory Comput.*, 2013, **9**, 4155.

48 V. M. Pereira, A. H. Castro Neto and N. M. R. Peres, *Phys. Rev. B: Condens. Matter Mater. Phys.*, 2009, **80**, 045401.

49 J. Bardeen and W. Shockley, *Phys. Rev.*, 1950, **80**, 72.

50 S. Bruzzone and G. Fiori, *Appl. Phys. Lett.*, 2011, **99**, 222108.

51 H. Lang, S. Zhang and Z. Liu, *Phys. Rev. B*, 2016, **94**, 235306.

52 T. Cheng, Z. Liu and Z. Liu, *J. Mater. Chem. C*, 2020, **8**, 13819.

53 D. Yu, Y. Zhang and F. Liu, *Phys. Rev. B: Condens. Matter Mater. Phys.*, 2008, **78**, 245204.

54 A. Delin, P. Ravindran, O. Eriksson and J. Wills, *Int. J. Quantum Chem.*, 1998, **69**, 349.

55 S. Z. Karazhanov, P. Ravindran, A. Kjekshus, H. Fjellvåg and B. G. Svensson, *Phys. Rev. B: Condens. Matter Mater. Phys.*, 2007, **75**, 155104.

56 H. Wang, G. Qin, J. Yang, Z. Qin, Y. Yao, Q. Wang and M. Hu, *J. Appl. Phys.*, 2019, **125**, 245104.

57 P. Ravindran, A. Delin, B. Johansson, O. Eriksson and J. M. Wills, *Phys. Rev. B: Condens. Matter Mater. Phys.*, 1999, **59**, 1776–1785.

58 D. R. Penn, *Phys. Rev.*, 1962, **128**, 2093.

59 L. Hedin, *Phys. Rev.*, 1965, **139**, A796.

60 E. E. Salpeter and H. A. Bethe, *Phys. Rev.*, 1951, **84**, 1232.